

Active Stability Observer using Artificial Neural Network for Intuitive Physical Human-Robot Interaction

Mohamed Amir Sassi¹, Martin J.-D. Otis^{1*}, Alexandre Campeau-Lecours²

¹ University of Quebec at Chicoutimi, Quebec, Canada, LAIMI Laboratory

² Laval University, Quebec, Canada, Robotic Laboratory

*Corresponding author: martin_otis@uqac.ca, 555 bd Universite (DSA), Chicoutimi, Québec, Canada, G7H 2B1

Abstract—Physical human-robot interaction may present an obstacle to transparency and operations’ intuitiveness. This barrier could occur due to the vibrations caused by a stiff environment interacting with the robotic mechanisms. In this regard, this paper aims to deal with the aforementioned issues while using an observer and an adaptive gain controller. The adaptation of the gain loop should be performed in all circumstances in order to maintain operators’ safety and operations’ intuitiveness. Hence, two approaches for detecting and then reducing vibrations will be introduced in this study as follows: 1) a statistical analysis of a sensor signal (force and velocity) and 2) a multilayer perceptron artificial neural network capable of compensating the first approach for ensuring vibrations identification in real time. Simulations and experimental results are then conducted and compared in order to evaluate the validity of the suggested approaches in minimizing vibrations.

Keywords—stability observer, vibrations identification, statistical analysis, artificial neural network, physical human-robot interaction, safety, transparency.

I. INTRODUCTION

Physical Human-Robot Interaction (pHRI) has become an interesting option in the industry for handling and assembling¹. In fact, it has a potential to produce a positive impact in assisting and sharing tasks in scheduling production and manufacturing activities while ensuring greater reliability, flexibility and precision²⁻⁴. However, robot’s stability and dynamic transparency may present a safety risk^{5, 6}. Indeed, physical contact with a force sensing handle could generate vibrations coming from an increase of the loop gain (i.e. vibrations generated by the approach of the poles toward the imaginary axis) which reduce performance, transparency and operations’ intuitiveness⁷. Thus, to remedy problems related to the application of this concept, several control models have been developed for reducing mechanical vibrations, and then ensuring safe and intuitive pHRI^{8, 9}.

Following a review of the art in technologies used for reducing vibrations and analyzing mechanisms’ stabilities, we will describe the primary contribution of this study; a design of an intelligent observer based on an artificial neural network approach for minimizing mechanical vibrations in pHRI in

real time. For that, we will begin by representing a model of a pHRI and its analysis based on an adaptive closed-loop control system. Moreover, two observers based on a statistical analysis and an artificial neural network will be elaborated for detecting and minimizing vibrations. These observers are evaluated and compared for different human arm stiffness’s. This evaluation provides a choice of an appropriate strategy for minimizing mechanical vibrations in pHRI.

II. RELATED WORK

This section is an introduction to the most used control and observers models, in the context of pHRI, aimed at satisfying mechanisms’ intuitiveness, performance and stability in all circumstances. First, we begin by presenting two types of control loops used in pHRI and then, we will finish with the neural network observers.

A. Impedance and Admittance Controls

Admittance and impedance controls are the most known control techniques in pHRI⁹. These techniques are applied in two different mechanisms. Impedance control is a force control model that takes a measurement of displacement as an input and reacts with a force as an output¹⁰. In contrast, admittance control takes a force as an input and reacts with a displacement as an output^{11, 12}. Furthermore, unlike admittance control, impedance control is the most common force control model used in the literature for mechanisms characterized by a low inertia and limited friction¹³. This last point makes the impedance control improper for collaborating with the Intelligent Assist Device (IAD) used in this work, since it is characterized by a high level of inertia and friction. These later make it too difficult for an operator to confer a movement to the IAD shown in both Fig. 1 and Fig. 2. An admittance controller with positional feedback is therefore preferred in this study.

To remedy issues of robotic mechanisms’ instabilities related to the human arm stiffness which is varying depending on the difficulty of the hand task⁹, some precursors, such as Tsumugiwa et al.¹⁴, explored an impedance control technique

to vary the damping coefficient. This addition of damping is based on the estimated value of the human arm stiffness. In the same context, Ikeura et al.¹⁵ used a variable impedance control method depending on the threshold of the mechanisms' velocity. In addition, Lecours et al.¹³ used a variable admittance control method based on human intentions inference while using the desired speed and acceleration. Furthermore, Corteville et al.¹⁶ detailed a technique using the admittance control based on an estimation of operators' planned movements. Finally, Duchaine et al.⁹ detailed a new approach of a robust controller aiming at ensuring a greater stability of interactive robotic mechanisms and intuitive interactions. Such improvement was done thanks to a combination of observer stability and a variable admittance control depending on human intentions.

B. Adaptive Controller using an Observer

Regarding the challenge of ensuring safe and intuitive pHRIs, one popular stability controller has been developed using the passivity approach. Such a solution has been used, principally, in haptics¹⁷ and, more recently, in the context of pHRIs^{9, 18}. The main idea is to ensure an efficient measurement of the device's energy flow. This measure provides an index to which we refer for accurate and efficient information on the system's state¹⁹. Thus, if mechanisms instability occurs, we can use a passive controller absorbing exactly the energy measured by an observer through a dissipative element (i.e. damping coefficient).

This tool has been used by several researchers in different applications. In fact, some studies used the concept of the passivity to guarantee the stability control of a teleoperation with force feedback^{20, 21}. Colgate et al.²² were interested in processing a virtual wall characterized by virtual settings such as stiffness and damping. Moreover, Hannaford et al.¹⁹ tested the passivity concept while doing a simulation and an implementation on a haptic device. Ryu et al.²³ have used the same principle introduced in¹⁹, but took into account the variation of the speed during a sample period. Similarly, Ryu et al.²⁴ called into question the principle of the passivity to ensure the stability of a commercial haptic device, labelled "PHANToM", while varying the desired energy threshold in the time. Furthermore, Ryu et al.²⁵ proposed a new approach consisting in realizing a stability observer able to detect haptic system instabilities through an analysis of its movements in the frequency domain. This observer may also quantify the instabilities' degree used thereafter by a stability controller to adapt a damping coefficient included in a dissipative element. However, these observers are not working with an admittance controller to move large payloads as demonstrated in our previous study²⁶. Indeed, this previous study has shown that the energy computation doesn't measure the increase of vibrations as a function of the human arm stiffness for the IAD. Therefore, we suggest an algorithm able to measure the quantity of vibrations in order to adapt the control parameters

such as the virtual mass and the gain loop. Routh–Hurwitz stability criterion was analyzed on the minimal virtual mass rendered at the end effector²⁷.

C. Artificial Neural Network Observer

One other solution for reducing mechanical vibrations is the so-called neural network vibration observer. This concept has been mainly used in detecting and minimizing vibrations affecting the normal lifetime of industrial equipment and causing the industry very high tooling costs. In this context, Rao et al.²⁸ studied the tool wear, surface roughness and vibrations of work pieces in boring of AISI 316 steel with cemented carbide tool inserts. For that, an experimental data acquisition of work pieces vibrations was conducted to a feed-forward four layered back propagation neural network. Thus, it was concluded that the proposed network model was a smart instrument for predicting the tool wear, surface roughness and amplitude of vibrations. Consequently, it will be possible to change tools at the correct time in order to get good quality of products and to minimize tooling costs.

Moreover, Barszcz et al.²⁹ were interested in developing a new approach for decreasing the cost of wind turbine maintenance. To do so, they tested an Adaptive Resonance Theory (ART) neural network as a tool for classifying vibration signals of bearing in gears in wind turbines. Furthermore, Kawabe et al.³⁰ proposed an active vibrations damping technique using a three layered neural network controller, a strain gauge sensor and an actuator in a longitudinal type cantilever beam. In this study, it was found that the neural network control system was robust against weight parameter variations. Afterwards, Ben Ali et al.³¹ explained a new approach for monitoring and diagnosing rolling element bearings to ensure the steadiness of industrial and domestic machineries. Therefore, a four layered neural network was constructed and trained with the recorded and the adjusted vibration signals. Based on these results, this paper suggests using the neural network as a stability observer in order to design an adaptive gain controller.

III. CONTRIBUTION

This paper presents simulations and experimental results on the stability of an IAD through an artificial neural network, labelled in the following Active Vibration Observer (AVO). This AVO is designed for measuring and then reducing mechanical vibrations, generated in pHRIs, below the threshold of the human perception. Such process could increase operator safety, transparency and operations' intuitiveness. The aforementioned observer will generate an index from a given signal with robustness to noise and human arm stiffness. This index will be used as a skillful means for performing an automatic adjustment of the control loop gain as a function of the detected mechanical vibrations in order to achieve our objectives in reducing such vibrations and in

avoiding performance's reductions in normal operations.

IV. MODELING HUMAN-ROBOT INTERACTION

The mathematical models used to represent the pHRI are presented below. First, the admittance transfer function is presented, then the IAD model is detailed and finally the closed-loop control strategy is developed.

A. Admittance Model

For ensuring greater transparency of the IAD which is coupled to a load, admittance model will be used. This model allows a force display (i.e. using a virtual mass and damping) that we want to be felt by the operators interacting with the robot instead of the real mass and damping. The one-dimensional second order differential equation, used in this study, is written as follows^{13, 27} (the IAD is supposed to be isotropic³²):

$$f_H = m_v(\ddot{x}_2 - \ddot{x}_0) + c_v(\dot{x}_2 - \dot{x}_0) + k_v(x_2 - x_0) \quad (1)$$

where f_H is the interaction force felt by the hand, m_v is the virtual mass, c_v is the virtual damping, x_0 is the equilibrium point and $x_2, \dot{x}_2, \ddot{x}_2$ are, respectively, the Cartesians position, velocity and acceleration of the load to move.

To simulate free motions, it is assumed that stiffness k_v , and equilibrium position x_0 , equilibrium velocity \dot{x}_0 and the equilibrium acceleration \ddot{x}_0 are set to zero. For this purpose, the second order differential equation is rewritten as follows²⁷:

$$f_H = m_v\ddot{x} + c_v\dot{x} \quad (2)$$

The desired velocity (set-point) can be written in the Laplace domain as follows^{27, 33}:

$$v_d(s) = \frac{F_H(s)}{m_v s + c_v} \quad (3)$$

where s is the Laplace variable, $v_d(s)$ and $F_H(s)$ are, respectively, the Laplace transforms of $\dot{x}(t)$ and $f_H(t)$.

The control scheme used in this work, is presented in Fig. 1^{27, 33} and the IAD is presented in Fig. 2. The operator, wishing to make a displacement via the robot model, generates a force measured by means of a force/torque sensor located in the handle, labelled sensing handle in Fig. 1. This measure, as well as the constrained velocity \hat{v}'_d according to safety limits computed at the previous time step (Fig. 1), are sent to the admittance model which will output a set-point velocity v_d to control according to (3). This desired velocity will be saturated using minimum and maximum values for safety purposes. The limited velocity \hat{v}_d is then sent to a velocity controller for ensuring a minimum steady state error. The

velocity controller used in this study is a proportional type. This choice was made to avoid the drawbacks of the increased acceleration noise due to the derivative gain and the decrease in the bandwidth due to the integral term (i.e. integral term is a sum so it will cause the accumulation of the error history from human input) when using a PID (i.e. classic control law). Finally, the resulting command will be sent to the IAD actuators outputting a measured velocity v_2 applied on the load M_R .

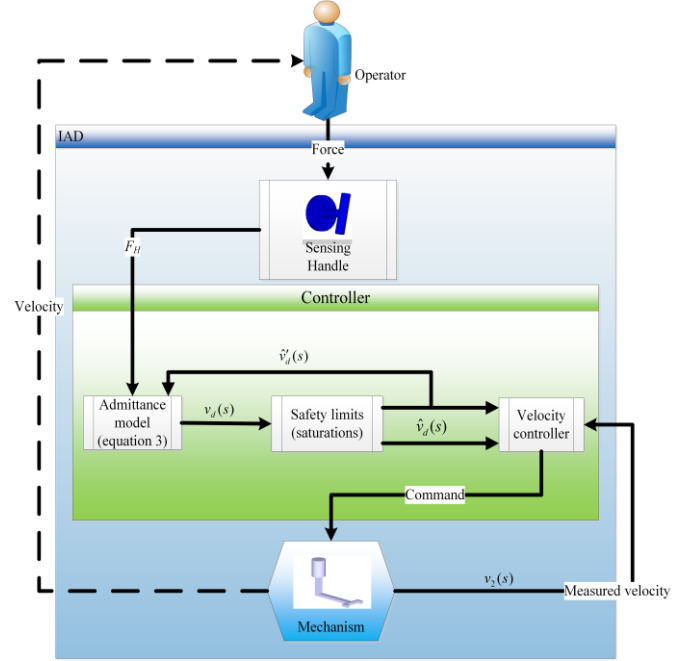


Fig. 1. Control scheme.

B. Robot Model

The robot model used for the experiments reported in this paper is the four-degree-of-freedom (4 DOF) IAD prototype allowing translation in all directions (XYZ, which are isotropic) and rotation about the vertical axis as seen in Fig. 2. The moving mass, approximately 500 kg, is in the direction of the X axis. Gravity is compensated using a balancing system with passive external mass (without control). The transmission between the actuators and the end-effector consists in a transmission belt as illustrated schematically in Fig. 2 and 3, where m_R is the motor-belt translation inertia and x_1 is its position, C_B is the mechanical transmission damping, K_B is the stiffness (i.e. C_B and K_B represent the transmission belt), C_R is the viscous friction generated when moving the load M_R , with the sensing handle, and x_2 is its position, v_2 is the measured velocity of the IAD in the feedback loop as shown in Fig. 4, F_H and F are, respectively, the interaction force (i.e. the force applied by the operator) and the actuation force sent to the IAD actuators and X_0 is the visual target desired by the operator.



Fig. 2. Intelligent Assistive Device (IAD)

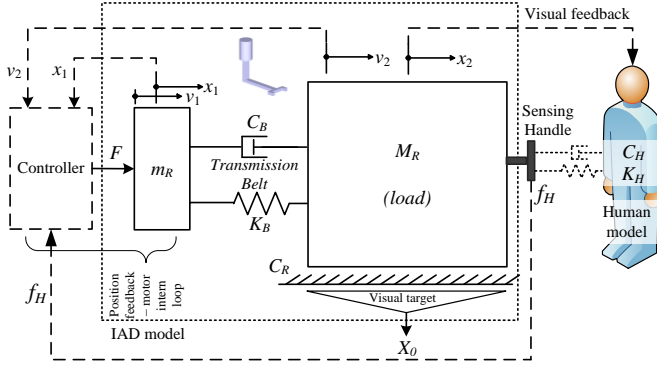


Fig. 3. Intelligent assist device model.

From Lecours et al. ⁸, the mechanical equations of this model are written as follows:

$$m_R \ddot{x}_1(t) + C_B \dot{x}_1(t) + K_B x_1(t) - C_B \dot{x}_2(t) - K_B x_2(t) = f(t) \quad (4)$$

$$M_R \ddot{x}_2(t) + K_B x_2(t) + (C_R + C_B) \dot{x}_2(t) - C_B \dot{x}_1(t) - K_B x_1(t) = 0 \quad (5)$$

Since the operator should not fell the load, (5) is equal to zero otherwise it's equal to $f_H(t)$. Thus, (4) and (5) lead to the following state space representation:

$$\begin{bmatrix} \dot{x}_1 \\ \dot{x}_2 \\ \ddot{x}_1 \\ \ddot{x}_2 \end{bmatrix} = \begin{bmatrix} 0 & 0 & 1 & 0 \\ 0 & 0 & 0 & 1 \\ -K_B & K_B & -C_B & C_B \\ \frac{m_R}{M_R} & \frac{m_R}{M_R} & \frac{m_R}{M_R} & \frac{m_R}{M_R} \\ \frac{K_B}{M_R} & \frac{-K_B}{M_R} & \frac{C_B}{M_R} & \frac{-(C_R + C_B)}{M_R} \end{bmatrix} \begin{bmatrix} x_1 \\ x_2 \\ v_1 \\ v_2 \end{bmatrix} + \begin{bmatrix} 0 \\ 0 \\ 1 \\ 0 \end{bmatrix} f \quad (6)$$

C. Suggested Control Loop Model

The suggested control loop model is represented in Fig. 4 ¹³. This model assumes that the operator acts as a spring-damping system where K_H is the operator stiffness and C_H is the operator damping coefficient ³⁴. This operator generates a force F_H as a function of the visual target. After that, F_H will be transferred to a desired velocity v_d by means of an admittance model, explained in (3). Moreover, a transfer function called *Imperfections* is also added where T represents a phase. This transfer function represents the effect of signal

filtering, the errors of robot dynamics modeling and small delays ¹³. The result of the *Imperfections* will be then sent to a velocity controller K_p (i.e. the control loop gain) which will be adjusted by our suggested algorithm. Finally, the resulting command F will be sent to the IAD actuators with a possible perturbation P (for example, when a moving part of the IAD touches an object not related to the load). Classical proportional-integral-derivative controller (PID) is not used here since stability analysis is only performed on the loop gain.

The transfer function of the closed-loop model shown in Fig. 4 can be written as follows:

$$\frac{V_2(s)}{F(s)} = \frac{sK_p(C_B s + K_B)(C_H s + K_H)}{a_6 s^6 + a_5 s^5 + a_4 s^4 + a_3 s^3 + a_2 s^2 + a_1 s + a_0} \quad (7)$$

where:

$$\begin{aligned} a_6 &= M_R T m_R m_v & (8) \\ a_5 &= M_R m_R m_v + M_R T C_B m_v + M_R T c_v m_R \\ &\quad + T C_B m_R m_v + T C_R m_R m_v \\ a_4 &= K_p M_R m_v + M_R C_B m_v + M_R c_v m_R \\ &\quad + C_B m_R m_v + C_R m_R m_v \\ &\quad + M_R T C_B c_v + M_R T K_B m_v \\ &\quad + T C_B C_R m_v + T C_B c_v m_R \\ &\quad + T C_R c_v m_R + T K_B m_R m_v \\ a_3 &= K_p M_R c_v + M_R C_B c_v + K_p C_B m_v \\ &\quad + K_p C_R m_v + M_R K_B m_v \\ &\quad + C_B C_R m_v + C_B c_v m_R \\ &\quad + C_R c_v m_R + K_B m_R m_v \\ &\quad + M_R T c_v K_B + T C_B C_R c_v \\ &\quad + T C_R K_B m_v + T c_v K_B m_R \\ a_2 &= K_p C_B C_H + K_p C_B c_v + K_p C_R c_v + M_R c_v K_B \\ &\quad + K_p K_B m_v + C_B C_R c_v \\ &\quad + C_R K_B m_v + c_v K_B m_R \\ &\quad + T C_R c_v K_B \\ a_1 &= K_p C_B K_H + K_p C_H K_B + K_p c_v K_B + C_R c_v K_B \\ a_0 &= K_p K_B K_H \end{aligned}$$

In the following, we will analyze the stability of the closed-loop transfer function, equation (7), using the position of its poles in the complex s-plane (i.e. complex plane on which Laplace transforms are graphed) along with the root locus stability criterion (i.e. graphical method for examining how the roots of a system change with variations of a certain system parameter which is in our case the operator stiffness K_H and the loop gain K_p). This latter is represented in Fig. 5 where the pole starting points are represented by a circle and the parameter variation is represented by a square.

Based on the result, shown in Fig. 5, we learn that greater operator stiffness leads to a more under-damped system. Accordingly, greater operator stiffness can lead to an unstable

system, however, in the most common situation, it leads to a vibratory system (i.e. poles become near to the imaginary axis). The system stability, here, is justified by the fact that the poles are located on the left-hand side (i.e. negative part) of

the Laplace plane. It should be pointed out that some of the poles shown in Fig. 5 correspond to high frequencies (30 rad/sec) and are very under-damped.

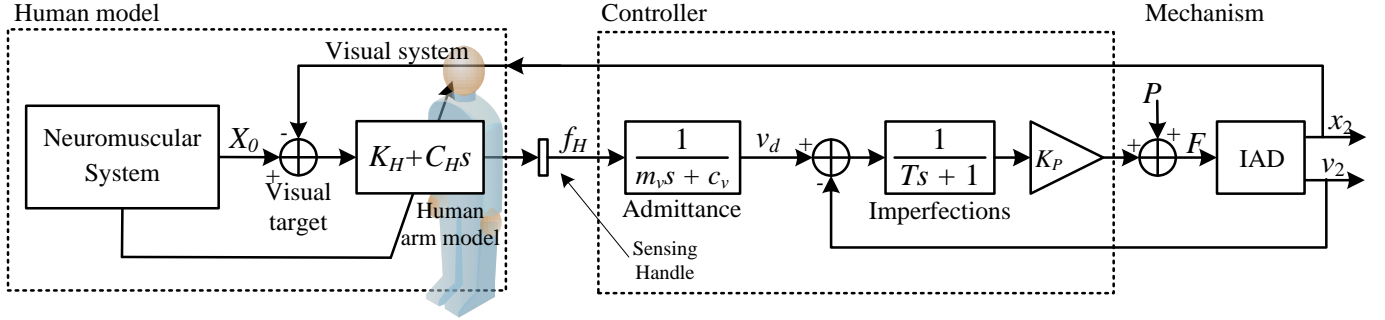


Fig. 4. Suggested control loop model without observers.

Thus, the operator will perceive the vibrations and then the interaction will be counterintuitive and uncomfortable. In fact, an increase of the loop gain (i.e. coming from an increase of the arm stiffness K_H) could move the poles to an unstable position.

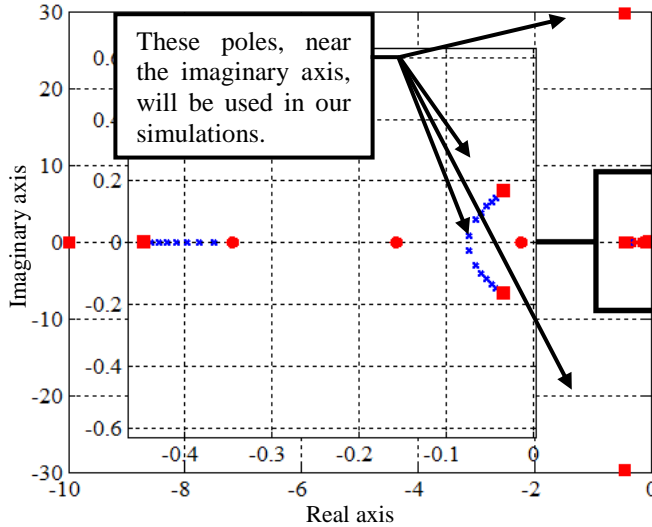


Fig. 5. Poles of the closed-loop model from equation (7) for an operator stiffness K_H , varying from 50 N/m (circle) to 850 N/m (square), $c = 20 Ns/m$, $T = 0.1 s$, $K_p = 10000$, $M_R = 500 kg$, $C_R = 100 Ns/m$, $m_R = 50 kg$, $K_B = 40000 N/m$, $C_B = 40 Ns/m$, $C_H = 23.45 Ns/m$. These values are taken from Lecours et al. ²⁷.

V. STABILITY OBSERVERS

This section discusses how to detect and reduce mechanical vibrations by observing the velocity signal (v_2) of a 1 DOF reduced-scale robot captured by means of a velocity sensor shown in Fig. 6. Hence, two approaches namely a statistical analysis, using both the time and the frequency domains, and an artificial neural network are presented below.

It should be pointed out that the velocity signal used to analyze the pHRI (i.e. vibrations and instability as described in the preceding sections) is captured from a 1 DOF robot

prototype (Fig. 6) allowing the translation only in the X direction and the moving mass is much more lower than the 4 DOF IAD prototype (Fig. 2) shown in Fig. 2 which allows much more higher vibrations frequencies. This analysis was first made to help us verify the validity of our algorithm. The stability analysis of this minimum phase system was previously presented in ²⁷.

A. Statistical Analysis

This analysis consists in assessing the electric signal representing the velocity of the movement of the mass in both the time and the frequency domains through a statistical analysis. For the frequency representation, the Discrete Fourier Transform (DFT) could be applied using the Fast Fourier Transform algorithm (FFT) which is known for its limited computation operations ²⁵ and its inability to deal with the problems that pose non stationary and non-periodic signals ³⁵. A Short Time Fast Fourier Transform (ST-FFT) is therefore preferred to analyze a short period of the signal through a Hamming sliding window.

The velocity signal and its transformation after filtering, used in this study, are shown in Fig. 7 where zone 1 and zone 3 correspond to a normal situation (i.e. without vibrations) and zone 2 corresponds to an abnormal situation (i.e. with vibrations). In zone 3, the handle is not held by the operator.

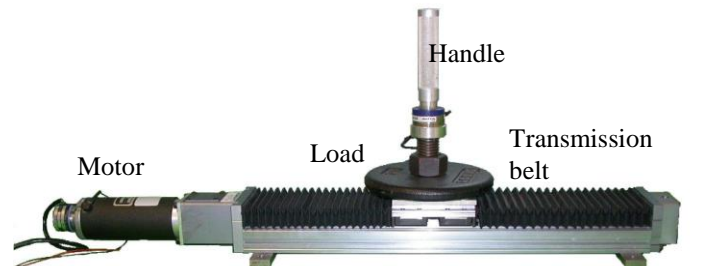


Fig. 6. 1DOF device used to evaluate the signal analysis prior to the IAD implementation

To analyze the dynamics and the frequency behaviors of the IAD with (6) and (7), we used the bode plot. This plot, represented in Fig. 8, shows the dynamics of the following four parts:

- The open loop transfer function (Fig. 8a));
- The closed loop transfer function (Fig. 8b));
- The human model transfer function (Fig. 8c));
- The IAD transfer function (Fig. 8d)).

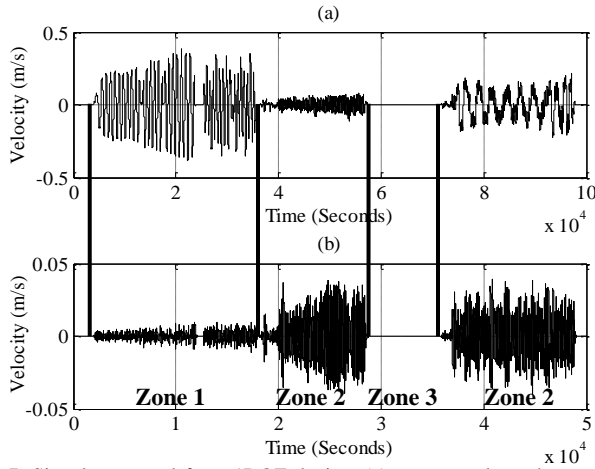


Fig. 7. Signal measured from IDOF device: (a) corresponds to the captured velocity signal and (b) represents its transformation after filtering (removing the arm movement) where zone 1 and zone 3 correspond to a vibrations-free situation and zone 2 corresponds to a vibratory situation.

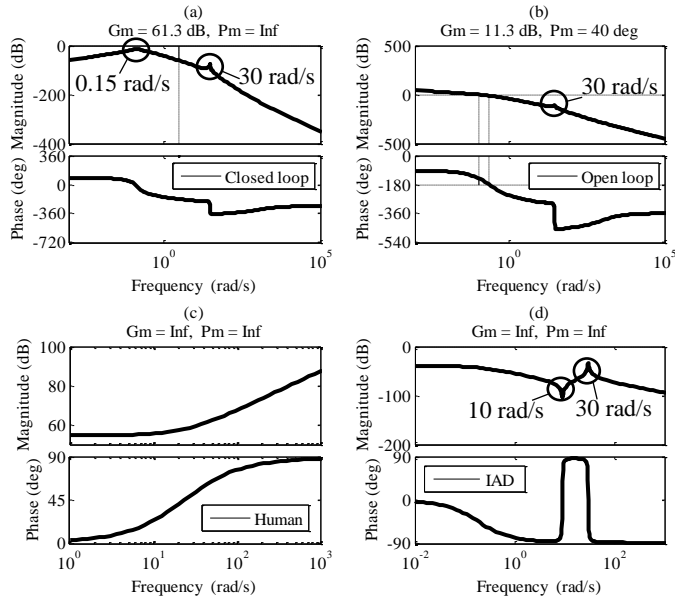


Fig. 8. Bode plots representing the dynamics of the closed loop control in (a), the open loop control in (b), the human in (c) and the IAD (without control) in (d). As described here, vibrations then should occur at 0.15 and 30 rad/s.

It is found that a resonance peak is present on the gains' curves of the closed loop, the open loop and the IAD which reflects the vibratory behavior created by the robot. Such behavior is driven by the presence of the human arm stiffness

in the control loop. In fact, the operator, wishing to control the manipulator of the robot, tends to increase the structural rigidity of his arm causing a decrease in the gain margin of the control loop which makes the poles closer to the imaginary axis. Thus, by approaching 0 dB at 180 degrees, the robot starts to vibrate at its resonant frequency.

Likewise, always aiming to effectively analyze the parts of the signal related to vibrations, it seemed to us very important to assess carefully the results of the ST-FFT. This latter was carried out under Simulink with a prior digitization of the signal (sampling frequency of 500Hz). It was performed with a length of 256 samples and a sliding Hamming window of length 128 samples with an overlap of 50%. The window's length is fixed by a reference to the system's dynamic to measure. These parameters are found experimentally.

Before such a procedure, the use of a filter was clearly essential for isolating vibrations frequencies from normal human motion and noise. Indeed, this filter will allow us, as a first step, to clarify the signal by reducing noise inherent to the global system distorting the analysis and, as a second step, to isolate the interesting parts containing vibrations. This filter was developed using the MatLab tool fdatool. Its nature was a band pass filter specified as a fourth order IIR Butterworth. After several adjustments, a filter with a band of [25.1 rad/s-189 rad/s] was chosen as a good filter for our signal processing objectives. The lower cutoff frequency is given by the maximum frequency response of the neuromuscular system³⁶. The upper cutoff frequency is fixed by the dynamic of the direct current (DC) motor; highest frequencies are related to noise. The result of the filtered signal is represented in Fig. 7(b).

The application of the ST-FFT allows us to clearly identify the frequency behaviors of the signal's parts related to normal situations and those related to abnormal situations. These results are represented in Fig. 9, where the solid line corresponds to the abnormal situations and the dashed line corresponds to the normal situation.

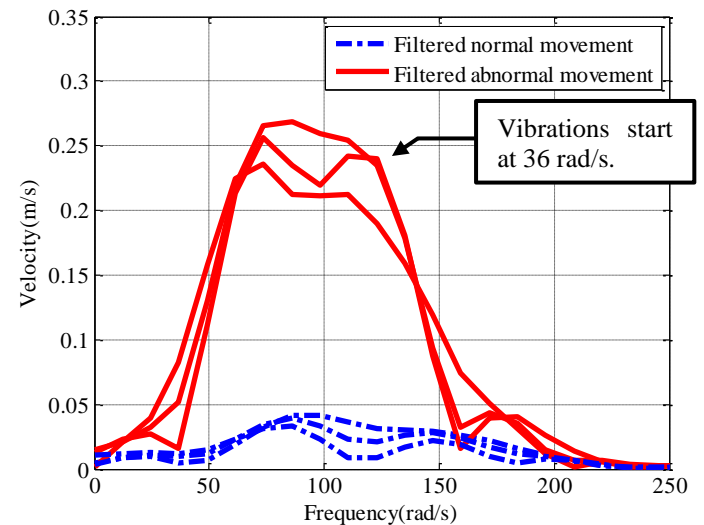


Fig. 9. Vibrations' identification with the 1 DOF robot prototype while using a Hamming sliding window.

The difference found between the resonant frequency in Fig. 8 (30 rad/s) and the vibrations frequency in Fig. 9 (36 rad/s) is coming from the fact that the 1 DOF reduce-scale robot has a lower mass than the 4 DOF IAD model. Our suggested mathematical model could be adequate, nevertheless, the identification is another issue not covered in this paper. Indeed, the goal is to find how much humans can increase the loop gain and then to reduce it by applying an adaptive gain controller. However, reducing the loop gain also decreases performance. Hence, the gain adjustment should be applied only when vibrations are perceived.

We note that humans could not control and manage high frequency vibrations, more than 31 rad/s, due to physical or cognitive limitations³⁷. This limitation forces them to increase the structural rigidity of their arms which appears as a hindrance to mechanisms' performance and operator safety, since it could generate vibrations. Hence, a trade-off between this natural limit and performance can be achieved by adjusting the control loop gain as a function of the identified vibrations. For achieving such identification, variance and standard deviation are used in this study as statistical variables applied in both time and frequency domains on the filtered velocity signal.

The variance and the standard deviation responses in the time and the frequency domains are represented in Fig. 10. In this figure, we can distinguish very clearly three areas in the signals in both the time and the frequency domains. In fact, we could see the first parts as well as specific frequencies controllable by the humans (zone 1 in Fig. 7), followed by those considered for them as out of control (zone 2 in Fig. 7) and finally, the spurious noises interspersed with inactive zones (zone 3 in Fig. 7).

As it was mentioned previously, the objective of this study is to identify, precisely, the parts of the signal related to vibrations in order to mitigate and to reduce them under the perception threshold of the humans. This can be achieved through judicious indexes able to update in real time the control loop gain K_p . The corresponding equations of these indexes, used in this study, are presented as follows:

$$I_1(t) = 1 - \alpha_1 \text{var}(STFFT(\hat{X})) \quad (9)$$

$$I_2(t) = 1 - \alpha_2 \text{var}(\hat{X}) \quad (10)$$

$$I_3(t) = 1 - \beta_1 \text{std}(\hat{X}) \quad (11)$$

$$I_4(t) = 1 - \beta_2 \text{std}(STFFT(\hat{X})) \quad (12)$$

where $\alpha_1, \alpha_2, \beta_1$ and $\beta_2 \in \mathbb{N}$, I_1 is the index of the variance in the frequency domain, I_2 represents the index of the variance in the time domain, I_3 represents the index of the standard deviation in the time domain, I_4 is the index of the standard deviation in the frequency domain and \hat{X} represents the filtered signal shown in Fig. 7(b).

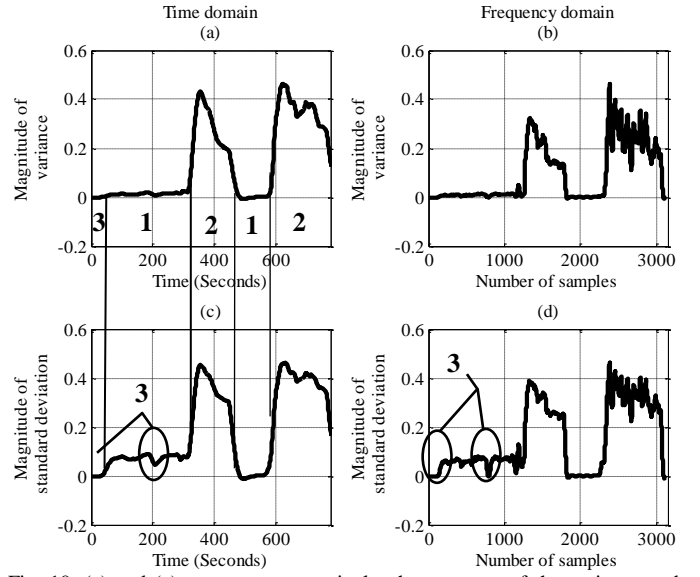


Fig. 10. (a) and (c) represent, respectively, the reponses of the variance and the standard deviation in the time domain and (b) and (d) represent, respectively, the reponses of the variance and the standard deviation in the frequency domain represented in sample using the factor: 256 (window length)/500Hz/2 (50% overlap) seconds.

The evolution of the indexes I_1, I_2, I_3 and I_4 is shown in Fig. 11.

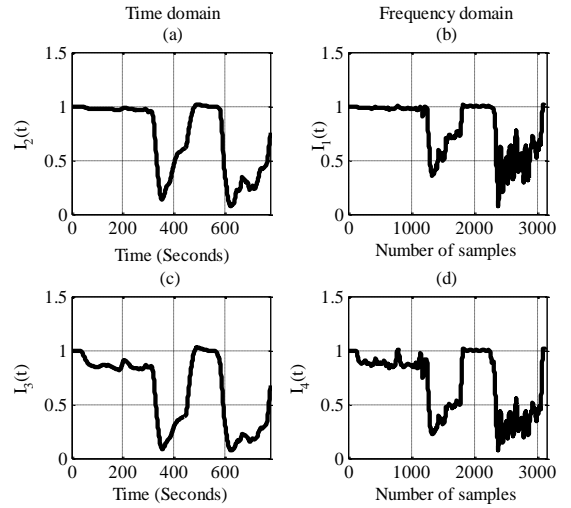


Fig. 11. (a) and (c) represent, respectively, the evolution of the variance index and the standard deviation index in the time domain (equations (10) and (11)) and (b) and (d) represent, respectively, the evolution of the variance index and the standard deviation index in the frequency domain (equations (9) and (12)) represented in sample using the factor: 256 (window length)/500Hz/2 (50% overlap) seconds.

Besides, we propose two other indexes using statistical characteristics, simultaneously, in the time and the frequency domains. These two indexes are obtained by the following equations where I_v represents the index of the variance observer and I_s represents the index of the standard deviation observer:

$$I_v(t) = 1 - \delta_1 \times (\text{var}(\hat{X}) + \text{var}(STFFT(\hat{X}))) \quad (13)$$

$$I_s(t) = 1 - \delta_2 \times (\text{std}(\hat{X}) + \text{std}(STFFT(\hat{X}))) \quad (14)$$

where δ_1 and $\delta_2 \in \mathbb{R}$.

The evolution of these two indexes is shown in Fig. 12(a) and Fig. 12(b).

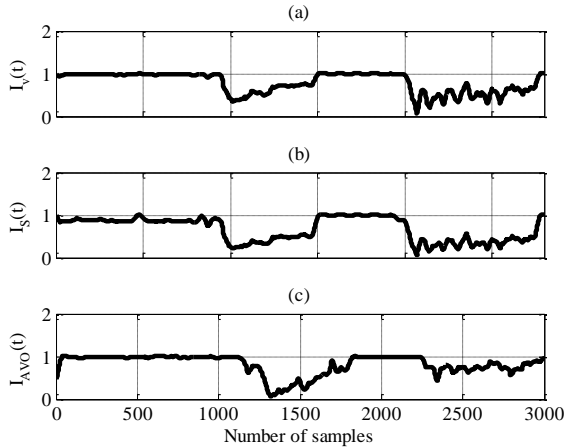


Fig. 12. Three different indexes for adjusting the control loop gain; (a) represents the evolution of the variance index in the time and the frequency domains, (b) represents the evolution of the standard deviation index in the time and the frequency domains and (c) represents the evolution of the Active Vibration Observer (AVO) index labelled I_{AVO} .

Based on these results, we notice that more the vibrations increase, more the indexes I_v and I_S decrease towards zero. In contrast, more the vibrations decrease, more the indexes tend towards one. Under these assumptions, we will use these indexes for the adjustment of the control loop gain for ensuring a reduction of the vibrations. Such improvement is ensured by a reduction of the control loop gain's value allowing the move away of the poles, shown in Fig. 5, from the imaginary axis (i.e. the source of vibrations). Thus, this gain will be updated according to the following law to achieve the best performance of the robot:

$$K_{p_n} = I \times K_{p_{n-1}} \quad (15)$$

where I could be the index I_v , I_S or I_{AVO} (i.e. the index I_{AVO} will be explained in the next section) and n represents the current time of the discrete clock.

B. Artificial Neural Network

The architecture of the most common and the most used network is the multilayer perceptron (MLP) ^{38, 39}. It is recognized as the first artificial system having a learning algorithm. In this sense, a two-layer feed-forward network with sigmoid hidden neurons and linear output neurons is created as shown in Fig. 13.

This artificial neural network is created as follows (i.e. ad-hoc method):

- The hidden layer contains 12 neurons;

- The output layer contains one neuron which returns a value for each sliding window.

For this type of classification, an MLP was trained and tested with a velocity signal coming from the 1 DOF reduce-scale robot. In fact, as it was mentioned before and shown in Fig. 7, there are two types of situations defined as follows:

- Normal situation (zones 1 and 3 in Fig. 7) in which no vibrations are observed;
- Abnormal situation (zone 2 in Fig. 7) in which vibrations are, clearly, present.

For each types of situation (normal and abnormal), we built 19 vectors corresponding to 19 segments of the signal, and each vector contains 128 values. Thereafter, we have combined all the vectors corresponding, respectively, to the first type of the situation and the second type of the situation (i.e. 38 vectors) in a matrix P of a dimension 128×38 . These dimensions are found experimentally. This matrix will be used as an input for training the artificial neural network shown in Fig. 13. Such procedure is known as a supervised learning.

The training of our artificial neural network is performed with the Levenberg-Marquardt backpropagation algorithm. It is known as the fastest backpropagation algorithm but the greediest in terms of memory. This training is carried out with different numbers of neurons in the hidden layer, namely 6, 8 and 10, ending finally with a number of 12. Throughout the tests, we kept the same number of iterations and the same learning rate.

A metaheuristic should be considered in this work, such as genetic algorithm, differential evolution or CMA-ES in order to optimize the ANN parameters (multiobjective optimization). Since the metaheuristic design is still complex when considering cross-validation (the number of k -fold), this paper presents only one solution after selecting experimentally different numbers of neurons. Any metaheuristic do not guarantee an optimal solution on such problem and the globally optimal solution is not trivial to find.

Therefore, our choice of the final architecture was based on the minimization of the Mean Square Error (MSE) criterion. In our case, the smallest value of the MSE was found with an MLP having 12 neurons in the hidden layer, which gives 4.94013×10^{-23} compared to 3.00628×10^{-2} in the 8 neurons configurations.

VI. EXPERIMENTAL RESULTS

First, we will evaluate the indexes of each observer, presented in this work, and we will assess their effects in the closed-loop when associated with the reduced-scale robot as a first step, and in a second step, the 4 DOF IAD model. This experimental investigation is done using Simulink RT-Workshop installed on a computer equipped with a processor Intel (R) Core™ i5-2430 M at 2.40 GHz and a RAM memory

of type DDR3 SDRAM with a capacity of 4 Gb at 609 MHz.

A. Real-Time Evaluation of the Indexes with the Reduced-Scale Robot

After training our artificial neural network, we tested it in

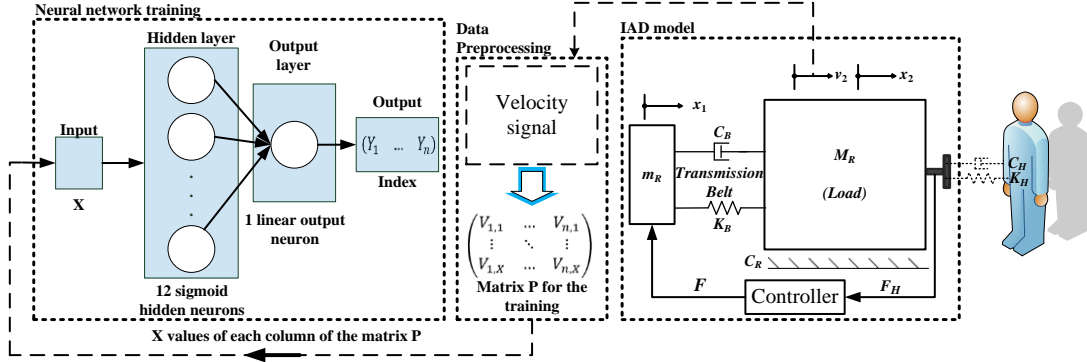


Fig. 13. Architecture and training of the artificial neural network.

By analyzing the Fig. 12(c), we notice a strong resemblance to Fig. 12(a) and Fig. 12(b). In fact, the index must be proportional to the vibrations' rate. This assumption means that more the vibrations increase, more the index approaches toward zero and more the vibrations decrease, more the index approaches to one.

B. Real-Time Evaluation of the Observers with the 4 DOF IAD Model

In the following, further analysis will be conducted in order to validate the best approach to adopt. To do so, experimental investigation on vibrations' detection and reduction has been carried out with three approaches. The first approach consists in a vibrations' detection and reduction via the AVO using two different velocity signals. The second approach consists in a vibrations' detection and reduction via the statistical analysis observer and, finally, the third approach consists in a vibrations' detection and reduction via another observer, labeled in the following Time Domain Vibration Observer Vibration Controller (TD-VOVC) already implemented in tested in ³³. This latter, generates an index by observing the local maximums and minimums of the mechanical vibrations in the velocity signal ¹³, which is difficult to adjust and tune.

Since the human arm stiffness varies ⁹ and a contact with a stiff environment is also a source of vibration ⁷, thus we varied the stiffness K_H during the simulation as shown in Fig. 15(a) (i.e. K_H is simulated as a square signal) from 50 to 850. The visual target X_0 obtained from the operator's neuromuscular system, was performed with a sinusoidal signal as an input to the closed loop shown in Fig. 15.

It should be emphasized that the following simulations are made with the 4 DOF IAD prototype (equation (7)).

Simulink with the same velocity signal used in the statistical analysis. To do so, we linked it to the output of the ST-FFT. Thus, the values included in the Hamming sliding window will be the neural network inputs. The response of the AVO is illustrated in Fig. 12(c).

Hence, we will not use the velocity signal used in the previous sections but we will use other velocity signals v_2 obtained from the simulations of the suggested control loop model, shown in Fig. 3 and Fig. 14. These simulated velocity (v_2) signals (from the model in Fig. 15) will be shown in the following sections.

Since the velocity signal has been changed, we should make some changes in the statistical analysis and the training of the artificial neural network.

For the statistical analysis all that we changed is the configuration of the ST-FFT and the analysis window. In fact, we changed the length of the aforementioned elements; they became a length of 500 samples, for the variance analysis, and 700 samples, for the standard deviation analysis. This increase of the windows length is coming from a decrease in the dynamic to measure since the inertia of the 4 DOF IAD model is higher than the 1 DOF reduced-scale robot. The results of this statistical analysis, when simulated with the simulated velocity signal are presented in Fig. 19(b) (i.e. the index of the variance observer, I_{SS}) and Fig. 20(b) (i.e. the index of the standard deviation observer I_{S-SS}). Regarding the training of the artificial neural network, we used the same procedure explained in the section artificial neural network but with some modifications. These modifications are explained in the following:

- For this type of classification, a two-layer feed-forward network with sigmoid hidden neurons and linear output neurons is created. This neural network is created with 10 neurons in the hidden layer and one neuron in the output layer, outputting a vector of a dimension 1×32 (i.e. the index I_{AVO-SS}). Afterward, this MLP was trained and tested with the simulated velocity signal (SS) represented in Fig. 16(a). Its result is shown in Fig. 16(b).

- Accordingly, we built for each type of situation (i.e. vibrations-free situation and vibratory situation) 16 vectors corresponding to 16 segments of the velocity signal and each vector contains 300 values. Subsequently, we established a matrix P, for the training of the artificial

neural network, of a dimension 300×32 (i.e. combination of the 16 vectors corresponding to each type of situation).

- The training of this artificial neural network was performed with the same algorithm which is the Levenberg-Marquardt backpropagation algorithm.

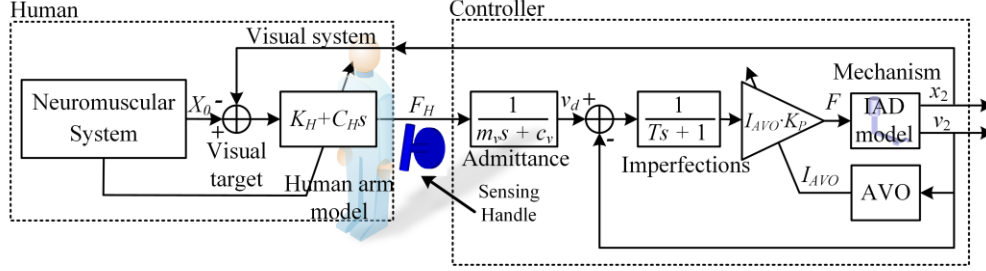


Fig. 14. Suggested control loop associated with the AVO.

Forthwith, after completing the necessary changes to accomplish the statistical analysis and the training of the artificial neural network with the simulated velocity signal, we may set forth the analysis part of the experimental investigation.

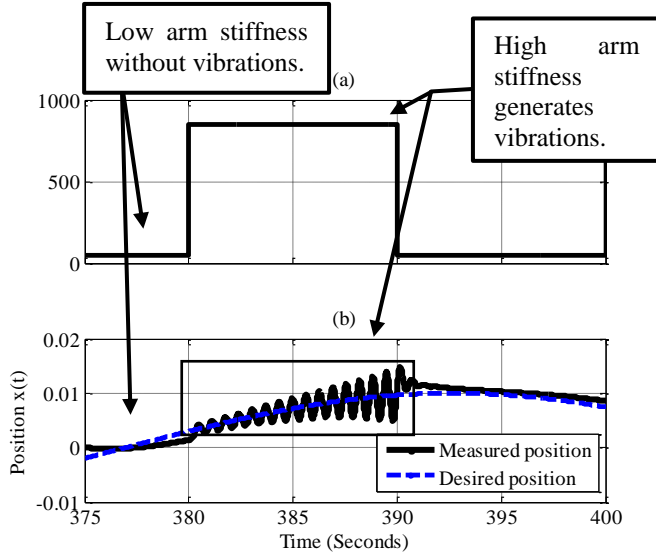


Fig. 15. (a) represents the evolution of the human arm stiffness going from 50 to 850 in a square waveform and (b) represents the response of the suggested control loop without the observers.

C. Feedback using the AVO

The first experimental investigation was conducted in three parts:

The first part of the investigation is a simulation of the control loop without the suggested observers, as was shown in Fig. 4. This test was first made to help us verify the capability of our observers, especially the AVO, in ensuring safe and comfortable interactions. The result of this simulation is shown in Fig. 15(b). In this figure we can distinguish, very clearly, the vibratory behavior caused by the human arm

stiffness. In fact, we notice that an increase in the arm stiffness increase the vibration (in this figure, the behavior is unstable: for a constant stiffness, the output increase). These results are consistent with the analysis presented previously and the results presented in ^{7, 9}. In fact, based on the result shown in Fig. 15(b), we can affirm that the human arm stiffness could destabilize the system. In our case, such vibrations are caused by the pole's located at 10 rad/s illustrated by the resonance peak shown in Fig. 8(d).

The second part of the investigation is a simulation of the suggested control loop associated with the AVO. The result of this simulation is presented in Fig. 16(c).

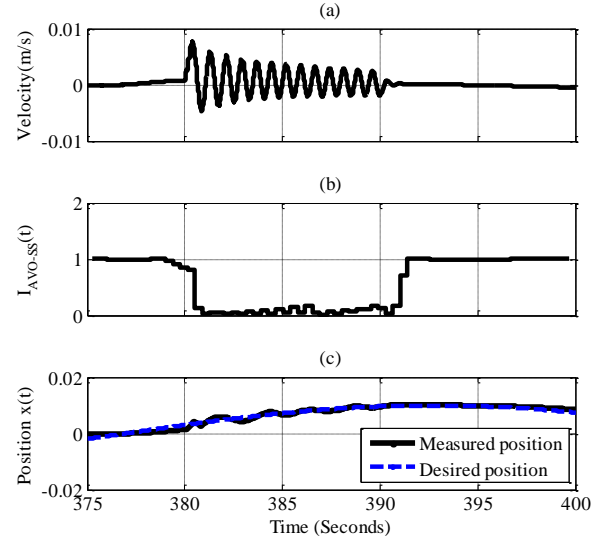


Fig. 16. (a) represents the simulated velocity (v_2) signal used as an input to the AVO, (b) represents the evolution of the AVO index labelled I_{AVO-SS} and (c) represents the response of the suggested control loop when associated with the I_{AVO-SS} .

The vibrations' detection and reduction task by the AVO is performed as follows:

- The index I_{AVO-SS} , shown in Fig. 16(b), is used to properly update the proportional gain K_p according to the update rule given by (15). This proportional gain decreases while the I_{AVO-SS} approaches to zero (i.e. when the AVO detects the vibratory situation) for ensuring vibrations' reduction in real time and then the stable interaction settles down;
- Thus, the I_{AVO-SS} increases to one (i.e. elimination of the vibrations: vibrations-free situation) and the proportional gain returns to its initial value (i.e. multiplication by one which is the value of the index when no vibratory behavior is detected);
- Finally, the proportional gain's update occurs in the same way whenever the AVO detects an unstable behavior (i.e. a vibratory situation).

Finally, the third part of the investigation is a simulation of the suggested control loop associated with the AVO but when this latter is exposed to another velocity signal shown in Fig. 17(b). This signal is resulting from a simulation of the closed loop when exposed to a force signal (with added noise), shown in Fig. 17(a), as an input to the admittance model.

To do so, we first begin by retraining the neural network with the simulated velocity signal. The training of the neural network was carried out with the same configuration of the previous neural network. Accordingly, our choice of the neural network was based on the minimization of the value of the MSE criterion. In fact, the smallest value of the MSE was found with an MLP having 10 neurons in the hidden layer, valued at 2.39952×10^{-25} . Such training results in an index $I_{AVO-SSF}$ shown in Fig. 17(c).

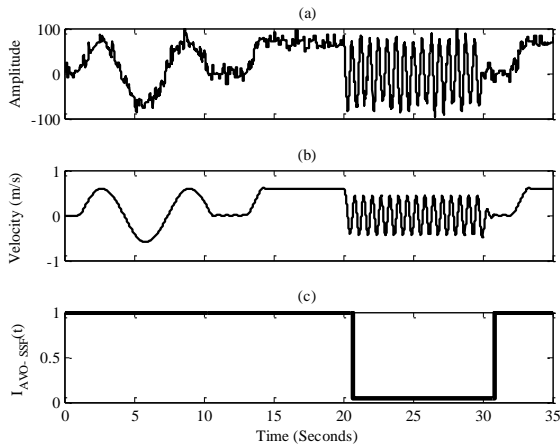


Fig. 17. (a) represents the force signal used as an input to the Admittance model with noise (noise power=10, over the worst case), (b) represents the simulated velocity signal used as an input to the AVO and (c) represents the evolution of the AVO index labelled $I_{AVO-SSF}$.

The system response when associated with this index in closed-loop is shown in Fig. 18 where the solid black line represents the velocity response of the suggested control loop

when associated with the $I_{AVO-SSF}$ and the dashed blue line represents the velocity response of the suggested control loop without the $I_{AVO-SSF}$.

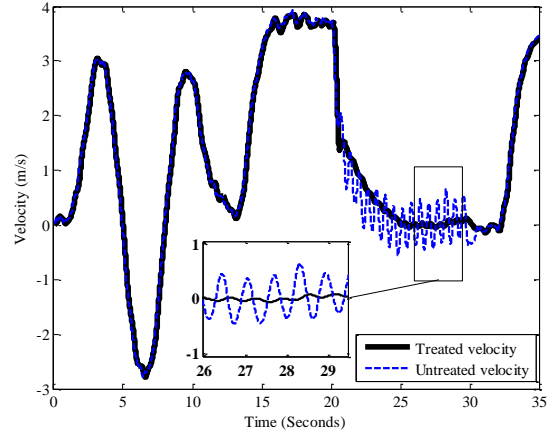


Fig. 18. The response of the suggested control loop when associated with the $I_{AVO-SSF}$ (solid black line) and the response of the suggested control loop without the AVO (dashed blue line).

Based on this result, we may conclude that the AVO index $I_{AVO-SSF}$ is able to reduce the mechanical vibrations in the electric signal. Indeed, by comparing the velocity answer of the system when associated with this index (i.e. the solid black line) to the velocity answer of the system without this index (i.e. the dashed blue line), we notice a significant decrease in the vibrations.

D. Feedback using Statistical Analysis Observer

We have replaced the index of the AVO in the closed loop by the index of the variance observer namely the index I_{SS} , shown in Fig. 19(b), in both the time and the frequency domains. The system response when associated with this index is shown in Fig. 19(c).

Likewise, we want to assess the ability of the standard deviation observer in reducing the vibrations in pHRIs. Thereby, we have replaced the previous index by the index of the standard deviation observer, I_{S-SS} , shown in Fig. 20(b), in both the time and the frequency domains. The system response when associated with this index is shown in Fig. 20(c).

Based on these responses, we can conclude that the indexes I_{SS} (variance) and I_{S-SS} (standard deviation) were able to reduce mechanical vibrations. Indeed, by comparing the answers of the system when associated with these two indexes to the system's answer presented in Fig. 15(b), we notice a significant decrease in the vibration amplitudes caused by an increase of the human arm stiffness.

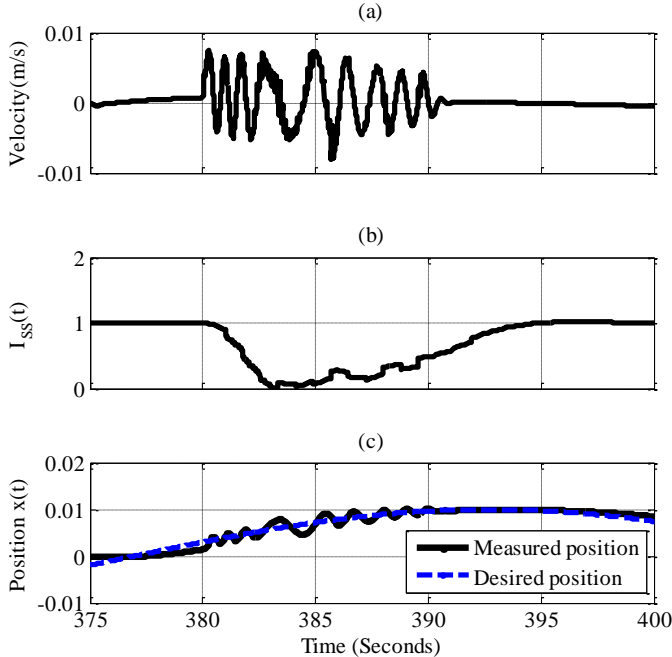


Fig. 19. (a) represents the simulated velocity signal used as an input to the variance observer, (b) represents the evolution of the variance index in the time and the frequency domains and (c) represents the response of the suggested control loop when associated with the I_{SS} .

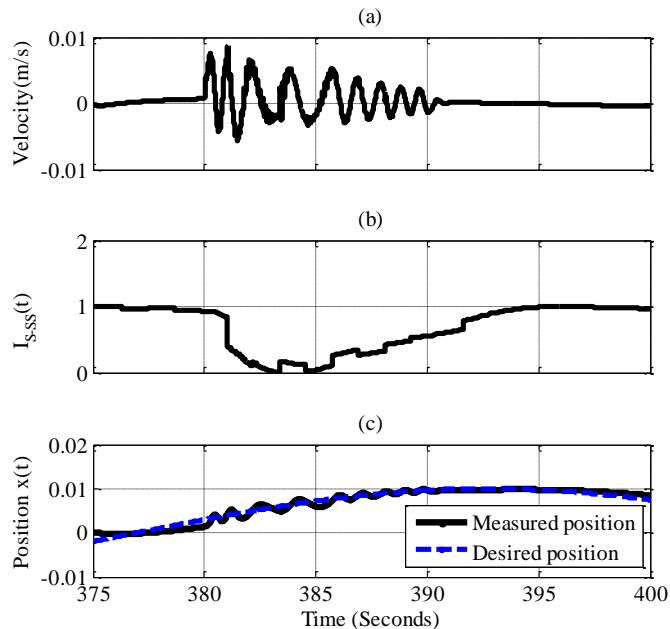


Fig. 20. (a) represents the simulated velocity signal used as an input to the standard deviation observer, (b) represents the evolution of the standard deviation index in the time and the frequency domains and (c) represents the response of the suggested control loop when associated with the I_{S-SS} .

E. Comparison with the TD-VOVC

For comparison purposes of our observers with other existing observers, the final experimental investigation was carried out with a different approach to those presented in this study. This approach, the TD-VOVC, is based on a detection

of the mechanical vibrations present in the signal through an observation of the vibrations' local maximums and minimums in the time domain³³. To do so, we have replaced the indexes of our observers by the TD-VOVC index, shown in Fig. 21(b). The response of the system when it is associated with this index is shown in Fig. 21(c).

VII. DISCUSSION

The most effective way to avoid hindrance to human performance and to ensure safe and intuitive pHRIs is to detect and eliminate the sources of vibrations. In this sense, the suggested observer, AVO, gives some encouraging simulation results thanks to its ability in detecting and preventing the vibratory behaviors. In fact, it was found that the AVO is capable of detecting in real time the vibrations when they occur due to the existence of the operator arm stiffness in the closed loop. The AVO performs this detection while generating an index I_{AVO-SS} when exposed to the simulated velocity signal shown in Fig. 16(a), and an index $I_{AVO-SSF}$ when exposed to the simulated velocity signal shown in Fig. 17(b). Indeed, when the vibrations are detected, the indexes tend to zero, otherwise they increase to one. Upon this, these indexes will be used in updating the proportional gain according to the aforementioned update rule (equation (15)), such that the gain introduced by the arm stiffness is cancelled by the AVO. Under this assumption, the loop gain becomes proportional to the I_{AVO-SS} and the $I_{AVO-SSF}$. When they decrease, the gain decreases for settling stable interactions by moving away the poles from the imaginary axis. Otherwise they increase to one and the gain returns to its initial value when no unstable behavior was detected (i.e. optimal operations).

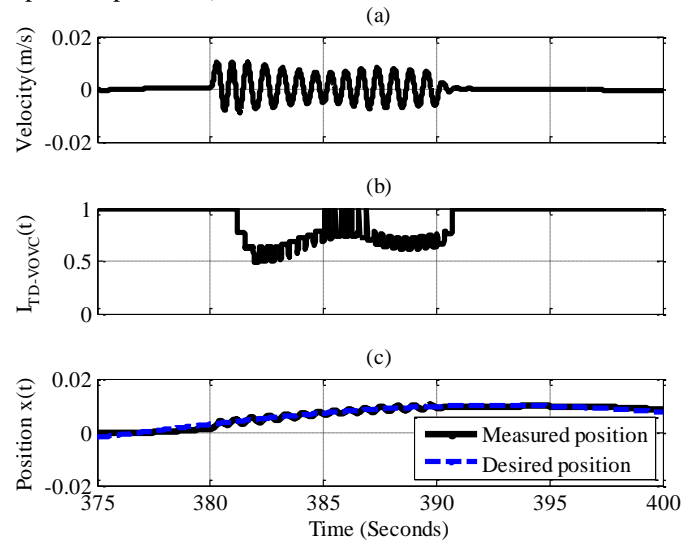


Fig. 21. (a) represents the simulated velocity signal used as an input to the TD-VOVC analysis observer, (b) represents the evolution of the index generated with the TD-VOVC approach and (c) represents the response of the suggested control loop when associated with $I_{TD-VOVC}$.

Furthermore, the statistical analysis observer explained above, as well as the approach based on vibrations' identification with references to local maximums and minimums (TD-VOVC), were also designed to reduce the mechanical vibrations distorting the operator's safety and the robot's stability and transparency but their performances were not enough for ensuring comfortable interactions.

Finally, since we have conducted several simulations with different approaches, one wants to know which one of them is the most appropriate for settling stable pHRIs. To do so, we have evaluated, for each approach, the robustness of the system by computing the error between the desired (x_0) and the measured (x_2) positions as shown in Fig. 22.

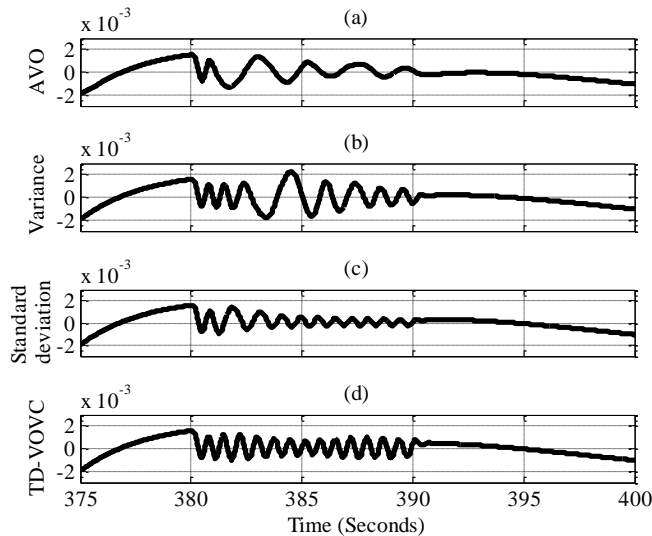


Fig. 22. The error ($x_2 - x_0$) evolution when the closed loop is associated with the AVO observer (a), with the variance observer (b), with the standard deviation observer (c) and with the TD-VOVC observer (d).

By analyzing the Fig. 22, we notice that the error between the desired and the measured positions, when the closed loop is associated with the AVO observer, is the one who has more tendency to converge to zero (i.e. minimization of the error) compared to the other errors (with lower frequency in the residual vibration).

In the following, further statistical analysis and performance analysis based on the execution times of each approach will be conducted to help us verify the validity of our algorithms and to affirm the aforementioned ascertainment. The statistical variable used in this investigation is the Standard deviation performed in a period of time between 380 and 390 seconds, exactly when the observers are activated (i.e. detection of a vibratory situation). The execution times will illustrate the time taken by each algorithm to perform a single treatment (i.e. one sample in the period of time between 380 and 390 seconds). The results of these analyzes are shown in Tab. 1 where the overhead presents the time taken to calculate all other blocks in the control loop (i.e. such as the IAD model, the human model,

the admittance and the imperfections models) and the time taken to ensure the additions, the multiplications and the starting as well as the closing of Simulink.

Based on these results, we notice that the lowest values of the statistical variable and the execution time, taken to perform a single treatment, are those obtained when the closed loop is associated with the AVO observer. From here, we may conclude that the AVO performs a better vibrations' identification and reduction and thereby ensures more comfortable and more intuitive interactions. Hence, we can confirm that the AVO is the most appropriate approach for ensuring intuitive, safe and comfortable pHRIs. We still need to improve those results with an evaluation with human participants. However, since we know the threshold perception of humans to vibrations in the glabrous skin⁴⁰, it would be possible to optimize the AVO under this threshold.

Table 1. Statistical and Performance Analyzes Results.

	AVO	Variance	Standard deviation	TD-VOVC
Statistical variable	Standard deviation	0.2941	0.5338	0.3443
		$\times 10^{-3}$	$\times 10^{-3}$	$\times 10^{-3}$
Execution times in seconds	Overhead	16.21	16.21	16.21
	Execution times of each treatment (each sample)	2.9199	7.7997	110
	$\times 10^{-5}$	$\times 10^{-5}$	$\times 10^{-5}$	320
				$\times 10^{-5}$

VIII. CONCLUSION

In order to ensure safe and intuitive pHRIs, vibratory behaviors should be detected and reduced under the human perception threshold. In fact, such behavior could decrease the operations' intuitiveness, robot's transparency and could increase the operator's safety risk. For that, two approaches have been presented for detecting and reducing the mechanical vibrations generated when collaborating with an IAD using an admittance control scheme. The first was a statistical analysis and the second was a multilayer perceptron artificial neural network. These approaches were designed in order to provide judicious indexes capable of ensuring an automatic update of the control loop gain as a function of the detected vibration amplitudes. Such adjustment could avoid hindrance to performance and intuitiveness in normal operations. Finally, based on our experimental results, we concluded that the AVO, based on an artificial neural network approach, provided an accurate detection and reduction of the

mechanical vibrations than the statistical analysis and the TD-VOVC approaches.

Future work will focus on an automatic optimization of the artificial neural network in order to find an optimal solution for any mechanism, considering a multiobjective optimization. Of course, the stability could be achieved using other solution such as an elastic actuator⁴¹ in order to control the equivalent stiffness of the human-robot interaction. Finally, a 3D haptic virtual guide for satisfying better pHRIs in assembly tasks will be used for the evaluation of the technology with participants.

Acknowledgments

This work is supported by the financial support of the *Fonds de recherche du Québec – Nature et technologies (FRQNT)*, under the grant number 2016-PR-188869. There is no conflict of interest regarding the methodology and the results presented in this paper.

References

1. AIEA. Matériel télécommandé et déclassement Les robots et les manipulateurs perfectionnés offrent de nouvelles possibilités. *IAEA Bulletin*. 1985; 27: 35-9.
2. Fallou O, Millet R, Creuchet S, Ranaivondrampola T and Chatila R. Le développement industriel futur de la robotique personnelle et de service en France. In: Nicole Merle-Lamoot GP, (ed.). 2012.
3. Oudeyer P-Y. Les grands défis de la robotique du 21e siècle. In: IRSEM, (ed.). Paris2009.
4. Martinez P, Coste F and Taravella A. Relation homme-robot: prise en compte des nouveaux facteurs sociologiques. In: Secuymind, (ed.). 2012.
5. Haddadin S, Albu-Schäffer A and Hirzinger G. Safety evaluation of physical human-robot interaction via crash-testing. *Robotics : Science and Systems Conference*. 2007, p. 217–24.
6. Zinn M, Khatib O, Roth B and Salisbury JK. Playing it safe [human friendly robots]. *Robotics & automation magazine - IEEE*. 2004; 11: 12-21.
7. Colgate E and Hogan N. An analysis of contact instability in terms of passive physical equivalents. *Robotics and automation - IEEE*. 1989; 1: 404-9.
8. Lecours A and Gosselin C. Computed-Torque Control of a Four-Degree-of-Freedom Admittance Controlled Intelligent Assist Device. *Experimental Robotics*. 2013; 88: 635-49.
9. Duchaine V and Gosselin C. Safe, Stable and Intuitive Control for Physical Human-Robot Interaction. *Robotics and Automation - IEEE*. 2009: 3383-8.
10. Carignan CR and Cleary KR. Closed-loop force control for haptic simulation of virtual environments. *Haptics-e*. 2000; 1: 1-14.
11. Hayward V and Maclean KE. Do it yourself haptics: part i. *Robotics & Automation Magazine, IEEE* 2007; 14: 88-104.
12. Linde RQvd and Lammertse P. Hapticmaster - a generic force controlled robot for human interaction. *Industrial Robot: An International Journal*. 2003; 30: 515-24.
13. Lecours A, Mayer-St-Onge B and Gosselin C. Variable admittance control of a four-degree-of-freedom intelligent assist device. *Robotics and Automation (ICRA), IEEE* 2012: 3903 - 8.
14. Tsumugiwa T, Yokogawa R and Hara K. Variable impedance control based on estimation of human arm stiffness for human-robot cooperative calligraphic task. *Robotics and Automation, IEEE*. 2002; 1.
15. Ikeura R and Inooka H. Variable impedance control of a robot for cooperation with a human. *Robotics and Automation, IEEE*. 1995; 3: 3097 - 102.
16. Corteville B, Aertbelien E, Bruyninckx H, Schutter JD and Brussel HV. Human-inspired robot assistant for fast point-to-point movements. *Robotics and Automation, IEEE*. 2007: 3639–44.
17. Ryu J-H, Kwon D-S and Hannaford B. Stability guaranteed control: time domain passivity approach. *Control Systems Technology*. 2004; 12: 860-8.
18. Albu-Schaffer A, Ott C and Hirzinger G. A Unified Passivity-based Control Framework for Position, Torque and Impedance Control of Flexible Joint Robots. *Journal of Robotics Research*. 2007; 26: 23.
19. Hannaford B and Ryu J-H. Time-Domain Passivity Control of Haptic Interfaces. *Robotics and Automation, IEEE*. 2002; 18: 1-10.
20. Anderson RJ and Spong MW. Asymptotic stability for force reflecting teleoperators with time delay. *The International Journal of Robotics Research*. 1992; 11: 135-49.
21. Niemeyer G and Slotine JJE. Stable adaptive teleoperation. *Oceanic Engineering, IEEE*. 1991; 16: 152-62.
22. Colgate E and Schenkel GG. Passivity of a class of sampled-data systems: Application to haptic interfaces. *Journal of Robotic Systems*. 1997; 14: 37-47.
23. Ryu J-H, Kim YS and Hannaford B. Sampled- and Continuous-Time Passivity and Stability of Virtual Environments. *Robotics, IEEE*. 2004; 20: 772-6.
24. Ryu J-H, Preusche C, Hannaford B and Hirzinger G. Time Domain Passivity Control With Reference Energy Following. *Control Systems Technology, IEEE* 2005; 13: 737-42.
25. Ryu D, Kang S, Kim M and Song JB. Frequency domain stability observer and active damping control for stable haptic interaction. *IET Control Theory Applications*. 2008; 2: 261-8.
26. Alexandre Campeau-Lecours, Martin Otis, Pierre-Luc Belzile and Clément Gosselin. A time-domain vibration observer and controller for physical human-robot interaction. *Mechatronics*. 2016; 36: 45–53.
27. Alexandre Lecours, Martin J.-D. Otis and Clément Gosselin. Modeling of physical human-robot interaction: Admittance controllers applied to intelligent assist devices with large payload. *International Journal of Advanced Robotic Systems*. 2016.
28. Rao KV, Murthy BSN and Rao NM. Prediction of cutting tool wear, surface roughness and vibration of work piece in

- boring of AISI 316 steel with artificial neural network. *Measurement*. 2014; 51: 63-70.
29. BARSZCZ T, BIELECKI A, WOJCIK M and BIELECKA M. Art-2 artificial neural networks applications for classification of vibration signals and operational states of wind turbines for intelligent monitoring. *Diagnostyka*. 2013; 14: 21-6.
30. Kawabe H, Tsukiyama N and Yoshida K. Active vibration damping based on neural network theory. *Materials Science and Engineering*. 2006; 442: 547-50.
31. Ali JB, Fnaiech N, Saidi L, Chebel-Morello B and Fnaiech F. Application of empirical mode decomposition and artificial neural network for automatic bearing fault diagnosis based on vibration signals. *Applied Acoustics*. 2015; 89: 16-27.
32. Gosselin C, Laliberte T, Mayer-St-Onge B, et al. A Friendly Beast of Burden: A Human-Assistive Robot for Handling Large Payloads. *IEEE Robotics & Automation Magazine*. 2013; 20: 139-47.
33. Campeau-Lecours A, Otis M, Belzile P-L and Gosselin C. A time-domain vibration observer and controller for physical human-robot interaction. *Mechatronics* 2016; 36: 45-53.
34. Duchaine V and Gosselin CM. Investigation of Human-Robot Interaction Stability Using Lyapunov Theory. *Robotics and Automation, IEEE*. 2008: 2189-94.
35. Dumas J. L'analyse temps – fréquence. In: technologies) d-SGM, (ed.). 2001.
36. Schouten AC, *, Vlugt Ed and Helm FCTvd. Design of Perturbation Signals for the Estimation of Proprioceptive Reflexes. *IEEE Transactions on Biomedical Engineering*. 2008; 55: 1612-9.
37. Jarrah M, Wassem W, Othman M and Gdeisat M. Human body model response to mechanical impulse. *Medical Engineering and Physics*. 1997; 19: 308-16.
38. Touzet C. Les réseaux de neurones artificiels introduction au connexionnisme. Neurosystèmes, Parc Scientifique Georges Besse, 30000 Nîmes., 1992.
39. Parizeau M. Réseaux de neurones GIF-21140 et GIF-64326. Université Laval, 2006.
40. Jones LA and Sarter NB. Tactile Displays: Guidance for Their Design and Application. *The Journal of the Human Factors and Ergonomics Society*. 2008; 50: 90-111.
41. Li X, Pan Y, Chen G and Yu H. Adaptive Human-Robot Interaction Control for Robots Driven by Series Elastic Actuators. *IEEE Transactions on Robotics*. 2017; 33: 169-82.